Atomically imaged crystal structure and normal-state properties of superconducting Ca_{10}Pt_{4}As_{8}((Fe_{1−x}Pt_{x})_{2}As_{2})_{5}

Zhen Wang, R. Jin, Lijun Wu, Jing Tao, A. B. Karki, J. Y. Pan, Yimei Zhu, and E. W. Plummer

Atomically Imaged Crystal Structure and Normal-State Properties of Superconducting $Ca_{10}Pt_4As_8((Fe_{1-x}Pt_x)_2As_2)_5$

Zhen Wang[1,2], R. Jin[1], Lijun Wu[2], Jing Tao[2], A. B. Karki[1], J. Y. Pan[1], Yimei Zhu[2], E. W. Plummer[1]

[1]Department of Physics and Astronomy, Louisiana State University, Baton Rouge, LA 70803

[2]Condensed Matter Physics and Materials Science Departement, Brookhaven National Laboratory, Upton, NY 11973

Abstract

Superconducting $Ca_{10}Pt_4As_8((Fe_2As_2)_5$ is rare because optimal superconducting transition temperature is achieved without chemical doping or pressure. However, the unclear crystal structure limits our ability to understand the structure-property relationship. Using atomically-resolved scanning transmission electron microscopy and electron diffraction, we directly determine the structure of this superconductor: it forms a monoclinic structure (space group $P2_1/n$) with lattice parameters $a = b = 8.76$ Å, $c = 20.18$ Å, and $\gamma = 90.5^o$. Compared with previously reported structures derived from diffraction experiments, the c lattice constant is doubled due to alternating stacking of Pt_4As_8 layers, which induces a high density of stacking faults. With the establishment of the crystal structure, stacking faults, and chemical composition, the distinctive normal-state electrical and thermal transport properties of our superconducting $Ca_{10}Pt_4As_8((Fe_{1-x}Pt_x)_2As_2)_5$ ($x \sim 0.05$) single crystals can be explained.

The discovery of high-temperature (T_c) superconductivity in Fe-based compounds has generated tremendous interest in the condensed matter and materials science community [1]. This class of materials offers opportunity not only for studying new superconducting mechanisms but also for exploring structure-property relationships and chemical doping effects [1]. As in high-T_c cuprates, Fe-pnictide superconductors form a layered structure, consisting of the FeAs building block, separated by interlayer spacers. Superconductivity can be induced by chemical doping, and the resultant phase diagrams are similar for both Fe- and Cu-based superconductors, i.e., superconductivity emerges after suppressing magnetism with increasing chemical doping [2,3]. One of few exceptions is $Ca_{10}Pt_4As_8(Fe_2As_2)_5$, which exhibits optimal T_c without chemical doping [4]. Structurally, the spacer $Ca_{10}Pt_4As_8$, between two adjacent FeAs layers, consists of an intermediary Pt_4As_8 layer, with the skutterudite structure, sandwiched by two Ca layers [4-7]. Unlike perovskite- or rocksalt-type blocking layers such as $Sr_4M_2O_6$ (M = Sc, Cr, V) [8-11], the Pt_4As_8 layer in $Ca_{10}Pt_4As_8(Fe_2As_2)_5$ is negatively charged [4,6,7]. This means that the Pt_4As_8 layer competes with neighboring negatively charged FeAs layer for electrons provided by Ca. As a result, atomic displacement and stoichiometry in $Ca_{10}Pt_4As_8(Fe_2As_2)_5$ is critical to both superconductivity and the normal-state physical properties [12,13]. Evidence is accumulating that subtle changes in either Ca or Pt distribution [12,14] or $FeAs_4$ tetrahedral distortion [13,14] would negatively impact superconductivity in $Ca_{10}Pt_4As_8(Fe_2As_2)_5$. For example, Pt vacancies in $Ca_{10}Pt_3As_8(Fe_2As_2)_5$ leads to the absence of superconductivity [5-7].

Complicating the interpretation is the fact that $Ca_{10}Pt_4As_8(Fe_2As_2)_5$ can form multiple structures. To date, three space groups, *P4/n* (tetragonal) [6,7], *P2₁/n* (monoclinic) [15], and *P_1* (triclinic) [4,5,7], have been reported for this compound using single crystal X-ray diffraction refinement and are listed in Table 1. At present, the role of crystal structure on physical properties, particularly on T_c, is unknown. While superconductivity is observed in both tetragonal and triclinic structures [4-7], physical properties of monoclinic $Ca_{10}Pt_4As_8(Fe_2As_2)_5$ have not been investigated. Here, we report on the crystal structure (monoclinic) and the effect of Pt doping of superconducting $Ca_{10}Pt_4As_8((Fe_{1-x}Pt_x)_2As_2)_5$ determined by scanning transmission electron microscopy (STEM) and electron diffraction. We demonstrate that atomically resolved STEM is an essential compliment to either X-ray or neutron diffraction. With the direct observation of the crystal structure, stacking faults, and Pt doping, the unusual electrical and thermal transport properties of $Ca_{10}Pt_4As_8((Fe_{1-x}Pt_x)_2As_2)_5$ can be explained. The structure-property relationship in this system is further discussed.

Formula	$(Ca_{10}Pt_{4-y}As_8)((Fe_{1-x}Pt_x)_2As_2)_5$					
Label	α -1048		β -1048		γ -1048	
crystal system	Tetragonal		Triclinic		Monoclinic	
References	[7]	[6]	[7]	[5]	[15]	**This work**
Space group	P 4/n	P 4/n	P $\bar{1}$	P $\bar{1}$	P 2_1/n	*P 2_1/n*
a (Å)	8.716	8.733	8.7382	8.719	8.7032	*8.76*
b (Å)			8.7387	8.727	8.7032	*8.76*
c (Å)	10.462	10.481	11.225	11.161	21.01	*20.18*
α	90°	90°	81.049°	99.04°	90°	*90°*
β	90°	90°	71.915°	108.21°	90°	*90°*
γ	90°	90°	89.980°	90.01°	90°	*~ 90.5°*
dopant Pt x	0	0.03	0.13	~ 0.18		*~ 0.05*
T_c	~35 K	27 K	~ 13 K	29 K		*~ 32 K*

Table 1: Summary of reported crystal structures of $Ca_{10}Pt_4As_8((Fe_{1-x}Pt_x)_2As_2)_5$ compound (denoted 1048) determined by single crystal X-ray diffraction refinement. The T_c and x values are included for each sample. The column at the right is our data from STEM.

For the growth of $Ca_{10}Pt_4As_8(Fe_2As_2)_5$ single crystals, stoichiometric amounts of high purity calcium shot (99.999 % Alfa Aesar), platinum powder (99.95 % Alfa Aesar), iron powder (99.95 % Alfa Aesar), and arsenic powder (99.999 % Alfa Aesar) are mixed in a ratio of 10 : 4 : 10 : 18, as reported previously [7]. The mixture is placed in an alumina crucible and sealed in a quartz tube under vacuum. The whole assembly is heated in a box furnace to 700 °C at a rate of 150 °C/h, and is held at this temperature for 5 h. It is then heated to 1100 °C at a rate of 80 °C/h. After holding at 1100 °C for 50 h, it is cooled to 1050 °C at a rate of 1.25 °C/h. It is then cooled to 500 °C at a rate of 5.5 °C/h, and finally cooled down to room temperature by turning off power. Shiny plate-like single crystals with typical dimensions of $4 \times 4 \times 0.2$ mm^3 were obtained without any additional processing.

The chemical composition of resultant crystals was determined by Energy Dispersive X-ray Spectroscopy (EDX) in a FEI Quanta 200 scanning microscope, and by simulating STEM intensities. Cross-sectional TEM samples were prepared using focused ion beam (FIB) with Ga$^+$ ions, and were further milled using Nanomill with Ar$^+$ ions to remove surface damage. All TEM experiments were performed on the 200 kV JEOL ARM electron microscope equipped with two aberration correctors and a cold field emission source. The atomically-resolved structure of crystals was obtained in high-angle annular dark-field (HAADF)-STEM imaging mode. The simulated diffraction patterns were calculated based on the Bloch wave method. The simulation of HAADF-STEM images is based on the multi-slice method. The HAADF detector was set with 67 and 275 mrad as inner and outer collection

angles. Thermal motion is considered in the calculations by adding random displacements to atoms from their sites using the Gaussian function with their corresponding Debye-Waller factors. The channeling effect of the incident electron beam propagating along atomic columns was also included. Sample thicknesses used in our simulation is ranging from 20 to 50 nm with a step of 10 nm.

Magnetic susceptibility measurement was carried in a *Quantum Design* Magnetic Property Measurement System. Electrical resistivity and thermal conductivity measurements were performed in a *Quantum Design* Physical Property Measurement System (PPMS) using the standard four-probe technique. Magnetoresistivity (MR) at a constant temperature are measured by sweeping magnetic field between -14 Tesla and +14 Tesla, and calculated using $MR_{ab} = \{[\rho_{ab}(+H) + \rho_{ab}(-H)]/2 - \rho_{ab}(0)]\}/\rho_{ab}(0)$.

Different crystal structures of $Ca_{10}Pt_4As_8((Fe_{1-x}Pt_x)_2As_2)_5$ can be distinguished by the morphology [7]: plate-like crystals possess tetragonal structure while needle-like crystals are triclinic. In both the tetragonal and triclinic cases, the lattice parameters *a* and *b* are similar (Table 1), but the relative positions of consecutive Pt_4As_8 layers are different as discussed later. For our plate-like crystals (see the inset of Fig. 1(f)), we conducted atomically-resolved HAADF-STEM imaging and electron diffraction to determine the structure. The structure is monoclinic P $2_1/n$ (# 13) with the lattice constants of *a* = *b* = 8.76 Å, *c* = 20.18 Å, and γ ~ 90.5º. As illustrated in Fig. 1(a-d), the *c* axis lattice parameter is nearly doubled compared to the reported results for the tetragonal and triclinic structures (see Table 1) [4-7]. The unit cell consists of two $(Fe_2As_2)_5$ and two $Ca_{10}Pt_4As_8$ layers, with stacking sequence of Pt_4As_8 – Ca – Fe_2As_2 – Ca – Pt_4As_8 – Ca – Fe_2As_2 – Ca – Pt_4As_8 layers, as can be seen in HAADF-STEM images in Figs. 1(b-d). Note that the Pt_4As_8 layer is very thin compared to the Fe_2As_2 layer. HAADF-STEM images are sensitive to heavy elements, where the intensity is proportional to the square of atomic number Z^2 [16]. The brightest spots correspond to Pt and the dimmest ones correspond to Ca ions, with the Fe_2As_2 layer located between the Ca planes. The HAADF-STEM image of Fig. 1(b) is obtained along the [210] direction, where the Fe and As atomic columns in the Fe_2As_2 layer can be clearly separated. The Fe_2As_2 layers are congruently stacked as can be seen in Fig. 1(b). The intensity profile in Fig. 1(b) shows a higher intensity of the Fe column than that of As column in the Fe_2As_2 layer, which is unexpected because the atomic number of As (Z = 33) is larger than that of Fe (Z = 26). Such behavior can be attributed to the existence of Pt with Z = 78, partially occupying the Fe site in the Fe_2As_2 layer. In the right-hand side of Fig. 1(b), we plot the intensity along the yellow

line in the HAADF-STEM image (in the left-hand side), and the simulated result (red line). Comparison of experimental and simulated HAADF-STEM images allows us to estimate that Pt doping level to be $x \sim 0.05 \pm 0.02$. This gives the chemical composition of $Ca_{10}Pt_{4.5}Fe_{9.5}As_{18}$, consistent with EDX measurements.

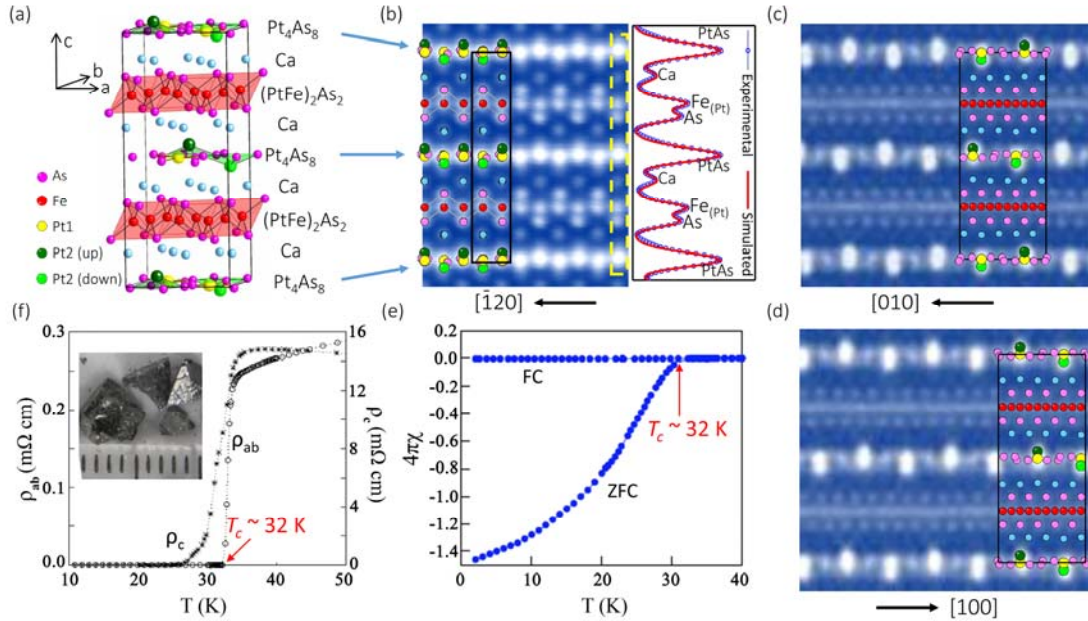**FIG. 1.** (Color online) (a) Crystal structure of $Ca_{10}Pt_4As_8((Fe_{1-x}Pt_x)_2As_2)_5$ with space group P $2_1/n$, presenting the doubling of $Ca_{10}Pt_4As_8((Fe_{1-x}Pt_x)_2As_2)_5$ viewed along the [210] (b), [010] (c) and [100] (d) directions, respectively. Structure models projected along corresponding directions are superimposed, with the color notation in (a), with in plane Pt denoted with yellow and out of plane by green respectively. The intensity scan in (b) shows the intensity along the yellow line in the HAADF-STEM image, and the red line represents the simulated result. (e) Magnetic susceptibility χ as a function of temperature measured under zero-field-cooling (ZFC) and field-cooling (FC) conditions. (f) Temperature dependence of both the in-plane (ρ_{ab}) and c-axis (ρ_c) resistivities. Inset: optical image of single crystals showing plate-like morphology.

Since there is no information about superconductivity in monoclinic $Ca_{10}Pt_4As_8(Fe_2As_2)_5$, would it still be superconducting? Figure 1(e) shows the temperature dependence of the magnetic susceptibility under both the zero-field-cooling (ZFC) and field-cooling (FC) conditions with the applied field of 20 Oe. Note that the system becomes diamagnetic below $T_c = 32$ K. At the same temperature, both the in-plane (ρ_{ab}) and c-axis (ρ_c) resistivities also drop to zero as shown in Figure 1(f). The data in Figs. 1(e) and (f) indicate that our single crystals are superconducting below 32 K. According to the phase diagram of T_c versus x for the tetragonal $Ca_{10}Pt_4As_8((Fe_{1-x}Pt_x)_2As_2)_5$ in Ref. [4], $T_c = 32$ K corresponds to $x \sim 0.02$, much lower than that estimated via EDX and STEM of 0.05 in our monoclinic sample. We also notice similar trend occurs for the triclinic $Ca_{10}Pt_4As_8((Fe_{1-0.13}Pt_{0.13})_2As_2)_5$ (

with $x \sim 0.13$) in which $T_c \sim 13$ K [7] would correspond to $x \sim 0.08$ of Pt doping in the T_c versus x diagram for the tetragonal structure [4]. These strongly suggest that superconductivity in both monoclinic and triclinic structures is less sensitive to Pt doping than that in the tetragonal phase.

Detailed features of the monoclinic structure of $Ca_{10}(Pt_4As_8)(Fe_{1.9}Pt_{0.1}As_2)_5$ are illustrated in Fig. 2. Figure 2(a) shows the structure in the ac plane, with the dashed blue square marking the middle Pt_4As_8 layer and adjacent Ca layers. Pt1 is in the plane and Pt2 are out of the plane (up and down). There is an obvious shift between the top and bottom Pt_4As_8 layers. For comparison, we depict the Pt_4As_8 layer in Fig. 2(b): it consists of distorted $PtAs_4$ squares with corner sharing As, which form As-As dimers as marked by dashed blue episodes. The unit cell of the $PtAs_4$ layer is indicated by the black square, which is larger than that of the Fe_2As_2 lattice marked by the light blue square in the bottom part of Fig. 2(b), with the side length $a_0 = 3.4$ Å. The relationship between the two unit cells is $a = b = \sqrt{5}a_0$. In each Pt_4As_8 layer, half of the $PtAs_4$ squares have Pt (Pt1, yellow color) atoms in the middle of the As_4 square. The other half Pt (Pt2, light and dark green colors) atoms are out of the plane, due to the adjacent Ca layer. Thus, the Pt2 atoms can be above (dark green) and below (light green) the Pt1 plane. The adjacent Ca atoms also shift to accommodate Pt2 atoms. Since Pt2 atoms are closer to As atoms in the adjacent Fe_2As_2 layer, the distortion of the Pt_4As_8 layer leads to the change of As-Fe-As bonding in the Fe_2As_2 layer. X-ray absorption fine-structure measurements indicate that stoichiometric $Ca_{10}(Pt_4As_8)(Fe_2As_2)_5$ consists of regular (non-distorted) $FeAs_4$ tetrahedron [13]. Such atomic arrangement may provide the optimal As-Fe-As angle ($\sim 109.5°$) for superconductivity [13-14,17-19].

Figure 2(c) illustrates possible relative positions between adjacent Pt_4As_8 layers. The Pt1 square lattice in one layer (solid red square) does not overlay with the lattice of the nearest Pt_4As_8 layer (dashed black square), The monoclinic structure of $Ca_{10}Pt_4As_8((Fe_{1-x}Pt_x)_2As_2)_5$ can be constructed from the tetragonal structure with the space group P4/n [4,6,7]: creating a supercell doubled along the c axis, and then sliding the middle Pt_4As_8 layer and adjacent Ca layers with a shift vector $q_B = (1/5, -2/5, 0)$ (variant B). Due to such shift, the symmetry of the system becomes monoclinic $P2_1/n$ with $\beta = 90.5°$. To further confirm this, we collected selected area electron diffraction (SAED) patterns from three main directions. Figure 3 shows both experimental (a-c) and simulated (d-f) SAED patterns, collected with a selected area aperture of 10 μm, along the [001], [210] and [010] zone-axis directions,

respectively. The consistency of the experimental and simulated diffraction patterns verifies the monoclinic structure.
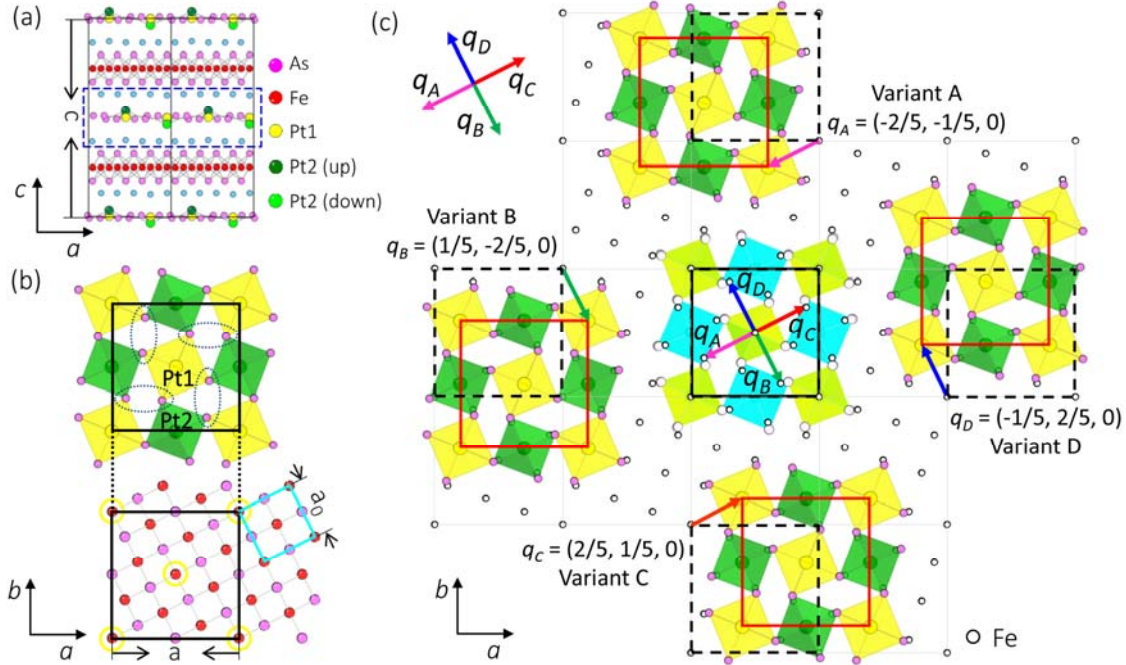

FIG. 2 (Color online) (a) Projected structure in the *ac* plane of monoclinic $Ca_{10}Pt_4As_8(Fe_2As_2)_5$: the solid square denotes the unit cell, and the dashed square marks the size of the middle Pt_4As_8 and adjacent Ca layers. (b) In-plane view of the Pt_4As_8 layer and the Fe_2As_2 layer. The black and blue squares represent the distorted Pt_4As_8 with $\sqrt{5} \times \sqrt{5}$ structure and the basic Fe_2As_2 unit cell with 1×1 structure, respectively. The yellow and green squares represent $PtAs_4$ with in-plane Pt1 (yellow) and off-plane Pt2 (green), respectively. The dashed ellipses represent As-As dimers. In-plane Pt1 is located right above the Fe site. (c) Four possible variants between adjacent Pt_4As_8 layers. Fe atoms in Fe_2As_2 layers are displayed as a reference.

As shown in Fig. 3, strong diffraction spots (indexed in yellow color) are associated with the basic tetragonal structure dictated by the Fe_2As_2 layer, while weak satellite reflections (indexed in blue color) mainly result from the distorted Pt_4As_8 structure. Compared with the simulated patterns, the satellite reflections are slightly different from the experiment: intensity difference in the a^*b^* plane (Fig. 3(a)) and the streaking along the c^* axis (Fig. 3(c)). As will be discussed later, such difference is induced by the stacking faults (SF) along the c axis.
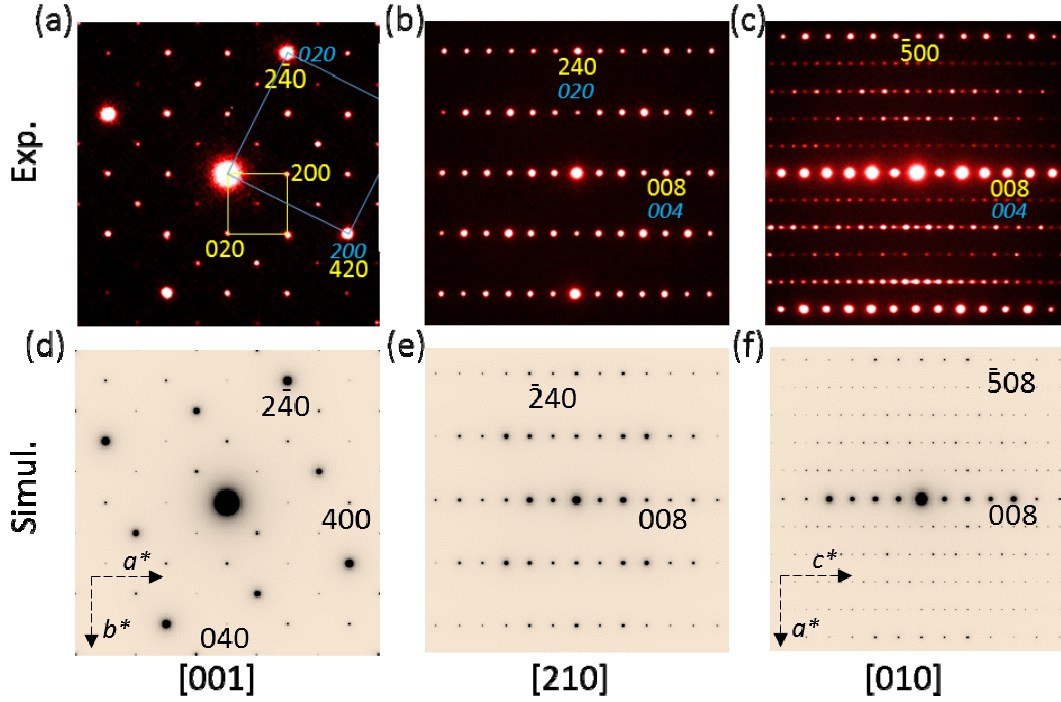
FIG. 3 (Color online) Experimental (a-c) and simulated (d-f) electron diffraction patterns along the [001], [210] and [010] directions, respectively. In (a-c), the electron diffractions are indexed with the monoclinic structure (yellow) and the basic Fe_2As_2 tetragonal structure (blue), respectively.

For tetragonal $Ca_{10}Pt_4As_8((Fe_{1-x}Pt_x)_2As_2)_5$, X-ray diffraction indicated superlattice reflections, which was considered to result from commensurability of Pt_4As_8 layers with Fe_2As_2 layers [6]. In addition, the superlattice structure was observed in the sister compound $Ca_{10}Pt_3As_8(Fe_2As_2)_5$ (Ca10-3-8) with the triclinic symmetry [5]. These observations suggest that the doubling of the unit cell is common in the $Ca_{10}Pt_nAs_8(Fe_2As_2)_5$ series (n = 3, 4). There are five possible variants (Fig. 2(c)) between two adjacent Pt_4As_8 layers, with shift vectors of q_A = (-2/5, -1/5, 0), q_B = (1/5, -2/5, 0), q_C = (2/5, 1/5, 0), q_D = (-1/5, 2/5, 0), and q_O = 0, i.e. without shifting. The structures reported by different groups (listed in Table 1) can be explained by the combination of the five variants. The tetragonal structure corresponds to the variant O case. The triclinic structure corresponds to one of four variants (A, B, C, D). The monoclinic structure in this work is the combination of variant A and variant C or variant B and variant D. When the five variants distribute randomly along the c axis, staking faults occur.

Figure 4 shows HAADF-STEM images in the ac plane defined in Fig. 2. The top panel Fig. 4(a) shows a region with low-density of SFs, and Fig. 4(b) represents a region with high-density. SFs occur along the c axis, as marked by green lines, while solid red rectangle

denotes the unit cell of our monoclinic structure. Note that Figs. 4(a) and (b) include three variants (B, C, D), with the difference clearly seen in Fig. 4(c). These variants are connected via either SFs as demonstrated in Fig. 4a (expanded area) or directly as shown in Fig. 4(b) (expanded area).

SFs are a common defect in layered materials. While SFs may be detected by diffraction techniques such as X-ray diffraction [20], detailed information can only be obtained via STEM as shown in Fig. 4, which reveals the distribution of SFs and their thicknesses and angles with respect to the regular structure. Clearly, stacking faults induce lattice distortions, creating strain [21], pinning [22], and charge redistribution [23] in the crystal. In Fig. 4(d), we plot the measured PtAs-PtAs layer spacing from the HAADF image in Fig. 4(b). The PtAs planar spacing shows slight changes (~1%) at SFs. These distortions will have marked impact on physical properties including superconducting transition temperature [17-28]. As a distortion-free system would result in the maximum T_c, the existence of SFs clearly reduces the superconducting transition temperature.
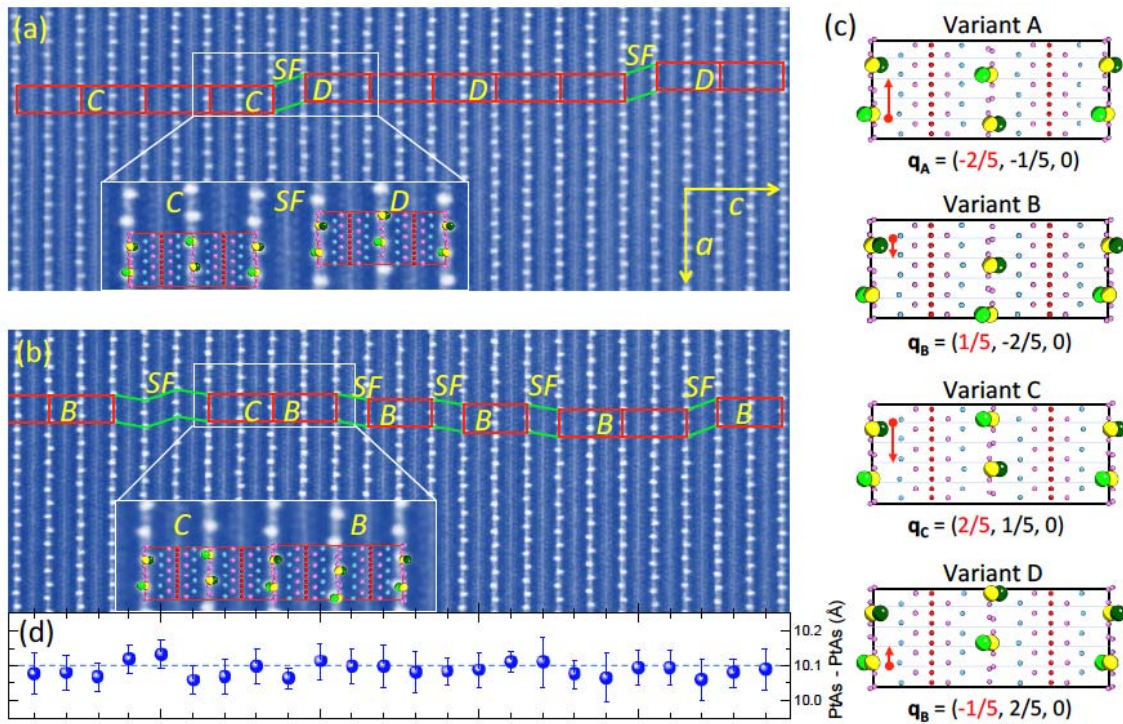

FIG. 4 (Color online) HAADF-STEM images of the *ac* plane obtained from two different areas representing low-density (a) and high-density (b) stacking faults (SF) marked by green lines. Enlarged images show the details of the SFs using the atomic color code in Fig. 1. (c) Projected structure in *ac* plane for the superstructures with four different variants. The shift component along *a*-direction is highlighted. The red squares mark the superstructures with A, B, and D variants, connecting by stacking faults with disordered variants. (d) The measured FePt layer spacing for Fig. 4(b).

Knowing the crystal structure and nature of the SFs. We can now interpret the physical properties of monoclinic $Ca_{10}Pt_4As_8((Fe_{1-x}Pt_x)_2As_2)_5$. Figure 5(a) shows the temperature dependence of both the in-plane (ρ_{ab}) and c-axis (ρ_c) resistivity of our $Ca_{10}Pt_4As_8((Fe_{1-x}Pt_x)_2As_2)_5$ single crystals, for the temperature range of 2 to 300 K. The overall profile of $\rho_{ab}(T)$ is similar to previous observation in samples with tetragonal and triclinic structures [5-6,29-30], i.e., $\rho_{ab}(T)$ decreases with decreasing T ($d\rho_{ab}/dT > 0$) in the entire temperature range in a quasi-concave fashion. Note that ρ_c also drops at T_c, but as was shown in Fig 1(f) the transition is much more gradual than that in the ab plane. This should be attributed to the imperfection of the sample along the c direction, including the large unit cell and SFs described above. More strikingly, ρ_c in the normal state increases with decreasing T, i.e., $d\rho_c/dT < 0$. This results in the increase of resistivity anisotropy $\gamma = \rho_c/\rho_{ab}$ from 17 at 300 K to 55 at 40 K as displayed in Fig. 5(b). The large ρ_c/ρ_{ab} makes $Ca_{10}Pt_4As_8((Fe_{1-x}Pt_x)_2As_2)_5$ one of the most anisotropic materials in the class of Fe-based superconductors [30-31]. The large anisotropy is most likely a result of directional disorder as discussed in Ref. [27].
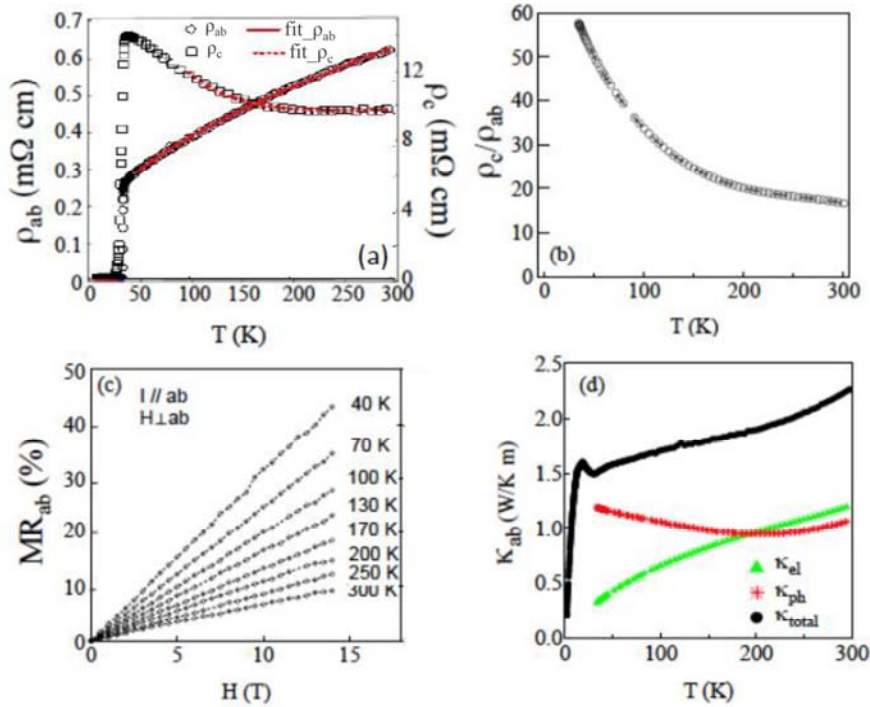

FIG. 5 (Color online) (a) Temperature dependence of ρ_{ab} and ρ_c of $Ca_{10}Pt_4As_8((Fe_{0.95}Pt_{0.05})_2As_2)_5$ single crystals, where solid and dashed lines are the fit to ρ_{ab} and ρ_c, respectively; (b) Temperature dependence of resistivity anisotropy ρ_c/ρ_{ab} in the normal state; (c) Magnetic field dependence of in-plane MR_{ab} at indicated temperatures and configuration. (c) Temperature dependence of in-plane thermal conductivity (black dots). In the normal state, both electron (triangles) and phonon (asterisks) contributions are estimated.

While ρ_{ab} shows metallic behavior, its temperature dependence in the normal state is rather unusual, i.e., neither linear nor quadratic as observed in other FeAs-based compounds [32]. Quantitatively, we find that the normal-state $\rho_{ab}(T)$ can be described by $\rho_{ab}(T) = A + B \sqrt{T}$ with $A = 0.079\pm0.009$ mΩ cm and $B = 0.267\pm0.002$ mΩ cm K$^{-1/2}$. The solid line in Fig. 4(a) is the fit to experimental data between 50 K and 300 K. Since all reported $\rho_{ab}(T)$ for $Ca_{10}Pt_4As_8((Fe_{1-x}Pt_x)_2As_2)_5$ has the similar temperature dependence regardless T_c value [5-6,30], we believe that the $\sqrt{T}$ dependence of ρ_{ab} is intrinsic to this material, and is insensitive to the crystal symmetry.

The non-metallic $\rho_c(T)$ can be fit using $A' + B' \sqrt{T} + C'/T$ with $A' = 2.6\pm0.5$ mΩ cm, $B' = 0.31\pm0.03$ mΩ cm K$^{-1/2}$, and $C' = 668\pm29$ mΩ cm K. The broken line in Fig. 5(a) is the fit to experimental data between 90 K and 300 K. The $\sqrt{T}$ term (second term) is clearly due to in-plane scattering, which can be intrinsic as Anderson proposed for high-T_c cuprates [33] and/or extrinsic due to stacking faults seen in our crystals (Fig. 4) [24]. The third term (T^{-1}-term) suggests incoherent interlayer scattering, similar to the case for underdoped high-T_c cuprates [33], $(Sr_4V_2O_6)Fe_2As_2$ [11], $NaFe_{1-x}Co_xAs$ [34], and underdoped $Ca_{10}Pt_3As_8(Fe_2As_2)_5$ [35].

It should be pointed out that the non-metallic $\rho_c(T)$ observed in our monoclinic $Ca_{10}Pt_4As_8((Fe_{0.95}Pt_{0.05})_2As_2)_5$ is unusual, as it is considered as an overdoped sample according to T_c versus x [4]. On the other hand, the $\sqrt{T}$ dependence of the electrical resistivity is normally expected at low temperatures in disordered metals and degenerate semiconductors because of interference with scattering by impurities [36-37]. For our sample, both SFs (Fig. 4) and partial substitution of Fe by Pt in the $(Fe_{1-x}Pt_x)_2As_2$ layer (Fig. 1b) should be major causes of disorder. As indicated by the T_c versus x in Ref. [4], disorder due to Pt doping disfavors superconductivity.

The anomalous in-plane electrical transport is further reflected in the magnetoresistance (MR). Figure 5(c) shows the magnetic field (H) dependence of in-plane (I//ab) MR$_{ab}$ with H $\perp$ ab at various temperatures above T_c. Note that, between 40 and 300 K, MR$_{ab}$ is positive, and increases with decreasing temperature at a fixed H. Remarkably, at each fixed temperature, MR$_{ab}$ exhibits linear-H dependence between 0 and 14 Tesla. According to the band theory for a single-band solid at the Fermi energy, MR is expected to depend quadratically on H at low fields and saturate at high fields [38]. For systems with multiple bands at the Fermi energy involving two types of charge carriers, the

11

magnetoresistance can be described by $MR = aH^2 / (b + cH^2)$ (where a, b, c are positive constants) [39]. For both one and two band models, a linear-H-dependent MR is unexpected, especially at low H. More recent theories have attempted to explain linear-H-dependent MR using classic [40-43], and quantum approaches [44]. The quantum MR becomes noticeable when $\hbar\omega_c \gg k_B T$ (where $\omega_c = eH/m^*$ is the cyclotron frequency), i.e., low T, high H, and small electron effective mass m^*. For $Ca_{10}Pt_4As_8((Fe_{1-x}Pt_x)_2As_2)_5$, the linear MR is unlikely due to the quantum effect because it persists to room temperature. According to Parish and Littlewood, linear MR can occur in disordered metals [41] and semiconductors [40] due to multiple scatterings of electrons by disorder.

A powerful probe of disorder effects is the thermal conductivity, as it is sensitive to lattice imperfection [45-50]. Figure 5(d) displays the temperature dependence of the in-plane thermal conductivity κ_{ab} between 2 and 300 K. In addition to an anomaly due to superconducting transition at T_c, the normal-state κ_{ab} is small for a single-crystal solid. We may estimate normal-state electronic contribution κ_{el} via the Wiedemann-Franz law with κ_{el} = $L_0 T/\rho_{ab}$ ($L_0 = 2.44 \times 10^{-8}$ V^2/K^2). As shown in Fig. 4(d) (green triangles), κ_{el} decreases with decreasing temperature in the normal state. As a result, the phonon contribution κ_{ph} (= κ_{ab} - κ_{el}) increases with decreasing temperature below ~ 250 K (see Fig. 4(d) (red asterisks)), as expected for a single-crystal solid. However, κ_{ph} is only around 1.0 W/K-m at room temperature, much lower than that for other FeAs-based layered compounds ($\geq$ 2 W/K-m) [51-52], as well as filled skutterudites (> 8 W/K-m) [45-46]. The low phonon thermal conductivity must be attributed to $Ca_{10}Pt_4As_8((Fe_{1-x}Pt_x)_2As_2)_5$ unique crystallographic structure: the insertion of the skutterudite Pt_4As_8 layer between Fe_2As_2 layers creates more two-dimensional structure as reflected by high anisotropy in resistivity. The dimensional confinement, large unit cell, stacking faults (plenary defects), and Pt substitution on the Fe site (point defects) can severely lower phonon contribution to the thermal conductivity by reducing phonon mean free path [47-50].

In summary, we have experimentally determined the structural, electrical, and thermal transport properties of superconducting $Ca_{10}Pt_4As_8((Fe_{1-x}Pt_x)_2As_2)_5$ single crystals with T_c = 32 K. Our high-resolution STEM images clearly reveal the structure with a doubling of the *c*-axis lattice parameter compared with the previously determined tetragonal and triclinic structures. Combined with electron diffraction, the crystal symmetry is identified to be monoclinic with the space group $P2_1/n$. STEM also provides direct evidence for Pt doping in

the Fe_2As_2 layer and indigenous stacking faults along the c axis. We find that the square-root temperature dependence and linear-field dependence of ρ_{ab}, non-metallic ρ_c, very low phonon thermal conductivity can be attributed to the unique structure of $Ca_{10}Pt_4As_8((Fe_{1-x}Pt_x)_2As_2)_5$ with large unit cell, stacking faults, and Pt doping in $(Fe_{1-x}Pt_x)_2As_2$ layers. The physical properties are very different from the individual building blocks as a consequence of the novel structure.

Acknowledgements

References

[1] For reviews, see J. Paglione, R. L. Greene, Nat. Phys. **6**, 645 (2010); A. A. Kordyuk, Low Temp. Phys. **38**, 888 (2012); H. Jiang, Y. L. Sun, Z. A. Xu, G. H. Cao, Chin. Phys. B **22**, 087410 (2013).

[2] I. I. Mazin, Nature **464**, 183 (2010).

[3] D. N. Basov, A. V. Chubukov, Nat. Phys. **7**, 272 (2011).

[4] T. Stürzer, G. Derondeau, D. Johrendt, Phys. Rev. B **86**, 060516(R) (2012).

[5] S. Kakiya, K. Kudo, Y. Nishikubo, K. Oku, E Nishibori, H. Sawa, T. Yamamoto, T. Nozaka, and M. Nohara, Journal of the Physical Society of Japan **80**, 093704 (2011).

[6] N. Ni, J. M. Allred, B. C. Chan, and R. J. Cava, PNAS **108**, E1019 (2011).

[7] C. Löhnert, T. Stürzer, M. Tegel, R. Frankovsky, G. Friederichs, D. Johrendt, Angew. Chem. Int. Ed. **50**, 9195 (2011).

[8] H. Ogino, Y. Matsumura, Y. Katsura, Koichi Ushiyama, S. Horii, K. Kishio and J.Shimoyama, Supercond. Sci. Technol. **22**, 075008 (2009).

[9] H. Ogino, Y. Katsura, S. Horii, Kohji Kishio and J. Shimoyama, Supercond. Sci. Technol. **22**, 085001 (2009).

[10] X. Zhu, F. Han, G. Mu, P. Cheng, B. Shen, B. Zeng, and H. H. Wen, Phys. Rev. B **79**, 220512(R) (2009).

[11] P. J. W. Moll, X. Zhu, P. Cheng, H. H. Wen, B. Batlogg, Nature Physics **10**, 644 (2014).

[12] J. Kim, H. Nam, G. Li, A. B. Karki, Z. Wang, Y. Zhu, C. –K. Shi, J. Zhang, R. Jin, E. W. Plummer, Sci. Rep. **6**, 35365 (2016).

[13] E. Paris, T. Wakita, O. Proux, T. Yokoya, K. Kudo, D. Mitsuoka, T. Kimura, K. Fujimura, N. Nishimoto, S. Ioka, M. Nohara, T. Mizokawa, and N. L. Saini, Phys. Rev. B **96**, 224507 (2017).

[14] E. Paris, B. Joseph, A. Iadecola, C. Marini, K. Kudo, D. Mitsuoka, M. Nohara, T. Mizokawa, and N. L. Saini, Phys. Rev. B **90**, 094508 (2014).

[15] T. Stürzer, Ph.D. thesis *(CaFeAs)$_{10}$Pt$_z$As$_8$ Superconductors and Related Compounds*, University of Munchen (2015).

[16] S. J. Pennycook, B. Rafferty, and P. D. Nellist, Microsc. Microanal. **6**, 343-352 (2000).

[17] S. Margadonna, Y. Takabayashi, Y. Ohishi, Y. Mizuguchi, Y. Takano, T. Kagayama, T. Nakagawa, M. Takata, and K. Prassides, Phys. Rev. B **80**, 064506 (2009).

[18] G. Garbarino, R. Weht, A. Sow, A. Sulpice, P. Toulemonde, M. Álvarez-Murga, P. Strobel, P. Bouvier, M. Mezouar, and M. Núñez-Regueiro, Phys. Rev. B **84**, 024510 (2011).

[19] K. Kobayashi, J. Yamaura, S. Iimura, S. Maki, H. Sagayama, R. Kumai, Y. Murakami, H. Takahashi, S. Matsuishi, H. Hosono, Sci. Rep. **6**, 39646 (2016).

[20] W. A. Phelan, D. C. Wallace, K. E. Arpino, J. R. NeilsoN, K. J. Livi, C. R. Seabourne, A. J. Scott, T. M. McQueen, JACS **135**, 5372 (2013).

[21] K. Szot, C. Rodenbucher, G. Bihlmayer, W. Speier, R. Ishikawa, N. Shibata, Y. Ikuhara, Crystals **8**, 241 (2018).

[22] A. -H. Puichaud, S. C. Wimbush, R. Knibbe, Supercond. Sci. Technol. **30**, 074005 (2017).

[23] S. Lei, H. Wang, L. Huang, Y. Y. Sun, S. Zhang, Nano Lett. **16**, 1317 (2016).

[24] R. Jin, H. R. Ott, D. P. Grindatto, Physica C **250**, 395 (1995).

[25] L. Wu, Y. Zhu, J. Tafto, D. O. Welch, M. Suenaga, Phys. Rev. B **66**, 104517 (2002).

[26] Z. Chen, F. Kametani, S. I. Kim, D. C. Larbalestier, H. W. Jang, K. J. Choi, C. B. Eom, J. App. Phys. **103**, 043913 (2008).

[27] Y. Yanase, J. Phys. Soc. Jpn. **79**, 084701 (2010).

[28] Q. Meng, A. S. Poyraz, A. C. Marschilok, E. S. Takeuchi, K. J. Takeuchi, G. Ceder, Y. Zhu, J. Am. Chem. Soc. **140**, 6961 (2018).

[29] Y. Kobayashi, T. Iida, K. Suzuki, T. Kawamata, M. Itoh, M. Sato, J. Phys. Soc. Jpn. **83**, 014712 (2014).

[30] Q.-P. Ding, Y. Tsuchiya, S. Mohan, T. Taen, Y. Nakajima, and T. Tamegai, Phys. Rev. B **85**, 104512 (2012).

[31] H. S. Ji, G. Lee, and J. H. Shim, Phys. Rev. B **84**, 054542 (2011).

[32] For a review, see T. Shibauchi, A. Carrington, Y. Matsuda, Annu. Rev. Condens. Matter Phys. **5**, 113 (2014).

[33] P. W. Anderson, *The Theory of Superconductivity in the High-T_c Cuprates* (Princeton University Press, Princeton 1997).

[34] N. Spyrison, M. A. Tanatar, K. Cho, Y. Song, P. Dai, C. Zhang, R. Prozorov, Phys. Rev. B **86**, 144528 (2012).

[35] J. Pan, A. B. Karki, E. W. Plummer, R. Jin, J. Phys.: Conden. Mat. **29**, 485702 (2017).

[36] B. L. Al'tshuler and A. G. Aronov, JETP Lett. **27**, 682 (1978).

[37] B. L. Al'tshuler, Sov. Phys. JETP **48**, 670 (1978).

[38] J. L. Olsen, *Electron Transport in Metals* (Interscience, New York, 1962).

[39] J. M. Ziman, *Principles of the Theory of Solids*, 2nd ed. (Cambridge Uni. Press, Cambridge 1972).

[40] M. M. Parish, P. B. Littlewood, Nature **426**, 162 (2003).

[41] M. M. Parish, P. B. Littlewood, Phys. Rev. B **72**, 094417 (2005).

[42] J. S. Hu, T. F. Rosenbaum, J. B. Betts, Phys. Rev. Lett. **95**, 186603 (2005).

[43] J. S. Hu, M. M. Parish, T. F. Rosenbaum, Phys. Rev. B **75**, 214203 (2007).

[44] A. A. Abrikosov, JETP **29**, 746 (1969); Phys. Rev. B **58**, 2788 (2000); Europhys. Lett. **49**, 789 (2003).

[45] G. S. Nolas, J. L. Cohn, G. A. Slack, Phys. Rev. B **58**, 164 (1998).

[46] X. Shi, J. Yang, J. R. Salvador, M. Chi, J. Y. Cho, H. Wang, S. Bai, J. Yang, W. Zhang, L. Chen, JACS **133**, 7837 (2011).

[47] V. Zlatic, A. C. Hewson, *Properties and Applications of Thermoelectric Materials: The Search for New Materials for Thermoelectric Devices* (Springer Science & Business Media 2009).

[48] M. S. Dresselhaus, G. Chen, M. Y. Tang, R. G. Yang, H. Lee, D. Z. Wang, Z. F. Ren, J. –P. Fleurial, P. Gogna, Adv. Mater. **19**, 1043 (2007).

[49] J. Garg, N. Bonini, B. Kozinsky, N. Marzari, Phys. Rev. Lett. **106**, 045901 (2011).

[50] K. T. Regner, D. P. Sellan, Z. Su, C. H. Amon, A. J. McGaughey, J. A. Malen, Nat. Commun. **4**, 1640 (2013).

[51] M. Tropeano, I. Pallecchi, M. R. Cimberle, C. Ferdeghini, G. Lamura, M. Vignolo, A. Martinelli, A. Palenzona and M. Putti, Supercond. Sci. Technol. **23**, 054001 (2010).

[52] M. A. McGuire, R. P. Hermann, A. S. Sefat, B. C. Sales, R. Jin, D. Mandrus, F. Grandjean, G. J. Long, New J. Phys. **11**, 025011 (2009).